Distribution of Kinetic Energy and Mixing in the Weddell Sea gravity current

Supplementary materials to the EGU Poster of the same name

Ole Pinner[*], Markus Janout,
Torsten Kanzow, Friederike Pollmann

April 24, 2023

Disclaimer

This text is still under construction and will be subject to changes in the future. As it is less revised than the poster, the probability of unclear wording and errors is also higher. The date above shows the last actualization of this document.

Link to the corresponding abstract[1]

[*]ole.pinner@awi.de

[1]https://doi.org/10.5194/egusphere-egu23-12417

Distribution of kinetic energy and mixing in the Weddell Sea gravity current

Ole Pinner[1], Markus Janout[1], Torsten Kanzow[1], Friederike Pollmann[2]

1.) Alfred-Wegener Institute, Bremerhaven, Germany
2.) Institute of Oceanography, University of Hamburg, Germany

TRR181

ALFRED-WEGENER-INSTITUT
HELMHOLTZ-ZENTRUM FÜR POLAR- UND MEERESFORSCHUNG

1. Introduction to the Weddell Sea

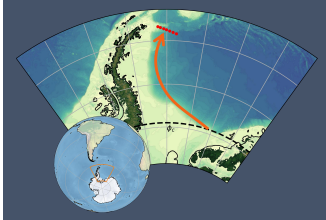

Due to climate change, the Antarctic Bottom Water warms increasingly. Global climate models cannot resolve the important small-scale mixing processes, therefore it is important to understand and quantify the mechanisms which determine the physical properties of the deep waters, as they are a vital part of the global thermohaline circulation.

The Weddell Sea is an important formation site of bottom water.

2. Measurements in the Gravity Current

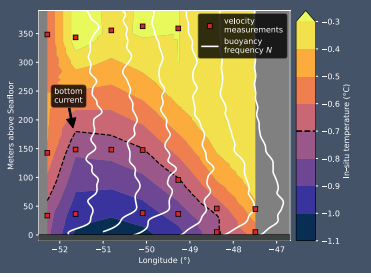

The dense Weddell Sea bottom water forms a gravity current that flows along the continental slope. The water column stratification is inferred from long-term temperature measurements and averages of CTD profiles. Mixing of the bottom current with the overlying warmer water determines the water properties of the deep water further down slope. We focus here only on internal wave mixing.

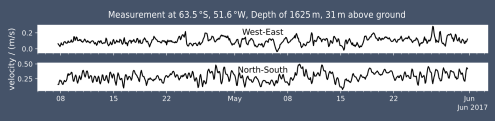

3. Wave Energy Levels

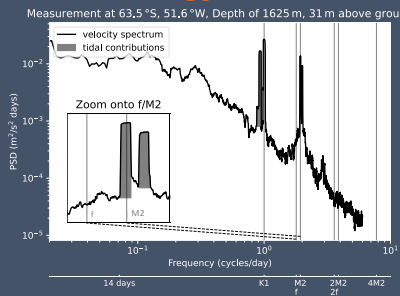

Integrating the power density spectra of the measured velocity time series yields the mean wave energy levels. The contributions of the internal wave continuum (between f and N) and internal tides can be calculated separately by isolating the tidal peaks. A distinction of barotropic and baroclinic tidal energy is possible through the depth dependency of measurements from the same water column.

4. Diapycnal Mixing

$$K_\rho \approx \frac{\Gamma}{1+\Gamma}\mu_0 f_e \frac{(m_\star/N)^2 E^2}{N^2}$$

Olbers & Eden, 2013

Buoyancy frequency	N	from CTD data
Energy level	E	from velocity spectra
Mixing efficiency	Γ	$= 0.2$
Coriolis frequency	f	$\approx -2.08 \times 10^{-5}$ Hz
Effective f	f_e	$= \lvert f \rvert \operatorname{arccosh}(N/\lvert f \rvert)$
Spectral bandwidth	$m_\star$	$= 0.01\,\mathrm{m}^{-1}$
	μ_0	$= 5/3$

We calculate the diapycnal diffusivity K_ρ, a measure of mixing, to quantify the effect of waves. But:

- Including baroclinic tides overestimates due to the prevalence of low tidal modes as their energy cannot be used for mixing directly.
- Excluding the baroclinic tides represents a conservative estimate of diffusivity.

Because the baroclinic tidal energy levels increase more in shallow waters than the wave continuum energy, the widest possible range of diffusivity coincides with the area of the highest mixing.

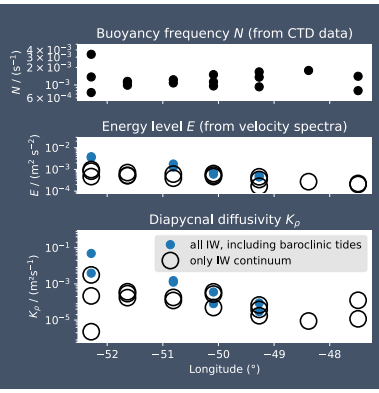

5. Take-Home Message

- Our results reveal the distribution of wave energy levels across the Weddell Sea bottom water gravity current. The internal wave mixing between the Weddell Sea Bottom Water and Warm Deep Water is around 2 orders of magnitude stronger in the shallower regions towards the Antarctic continent.
- The largest relative and absolute tidal contribution to the wave mixing is on the shelf. There, the possibility of underestimating the internal mixing by disregarding internal tides is especially prevalent.
- The next step is to place these results in context with estimates for the total mixing from Thorpe scales and finestructure in CTD profiles.

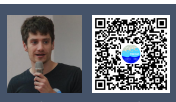

Ole.Pinner@awi.de

Sharing is encouraged

EGU

EGU Abstract & Voting

Contents

1 Introduction **4**

2 The Weddell Sea **4**

3 Mooring and CTD Data set **8**

4 Energy levels **10**
4.1 Internal Tides vs Internal Wave continuum 10
4.2 Barotropic vs Baroclinic tides 11
4.3 Distribution of Kinetic Energy 12

5 Buoyancy frequency N **14**

6 Diapycnal Diffusivity **16**

7 Conclusion **18**

8 References **19**

1 Introduction

Due to climate change, the Antarctic Bottom Water (AABW) warms and freshends increasingly [Menezes et al., 2017]. The Weddell Sea, a marginal sea in the Southern Ocean, is an important formation cite for AABW. Dense water is created under the ice shelf and during sea ice formation, and flows as a gravity current along the continental shelf into the deep sea. Mixing of the bottom current with the overlying warmer water determines the water properties of the deep water further down slope. Global climate models cannot resolve the important small-scale mixing processes, therefore it is important to understand and quantify the mechanisms which determine the physical properties of the down slope deep waters, as they are a vital part of the global thermohaline circulation [Lenton et al., 2008].

We focus here only on one possible mixing mechanism, namely internal wave mixing, also due to limitations of the available data. The Weddell Sea is strongly tidal, but knowledge about the interaction of gravity currents and internal waves is very limited. So before estimating the importance of wave mixing for the Bottom water formation, a description of internal wave background is first needed. Global Maps of internal wave energy do not reach further south than 60 °S, e.g. [de Lavergne et al., 2019, Pollmann, 2020] and cannot be used here. We quantify here the kinetic energy levels across the Antarctic continental slope, thereby distinguishing between the barotropic and baroclinic tides, and the internal continuum between the Coriolis frequency f and an average buoyancy or Brunt-Väisälä frequency N. After this we can compute diapycnal diffusivities and compare these results with literature values for mixing further up or down slope or for similar scenarios.

We hope that our result of which energy sources in the wave mixing and which parts of the continental slope are the most important, aids in the further understanding of Antarctic Bottom Water formation.

2 The Weddell Sea

The Weddell Sea is a large marginal sea in the Southern Ocean, bounded by the Antarctic peninsula in the east, the Filcher-Ronne Shelf in the south and the Antarctic Ice sheet in the west and in parts by the Scotia Sea in the north.

The Weddell gyre and the Antarctic slope front are the most import surface layer currents, but will not be considered here, as our research focus is on process above the sea floor. Because the Weddell Sea is an important formation site of Antarctic Bottom Water, its influences reach beyond the local level. he Weddell Sea bottom water gravity current connects the high salinity shelf water at the Filchner-Ronne and Larsen ice shelves to the Antarctic Bottom Water in the Southern Ocean. As we are

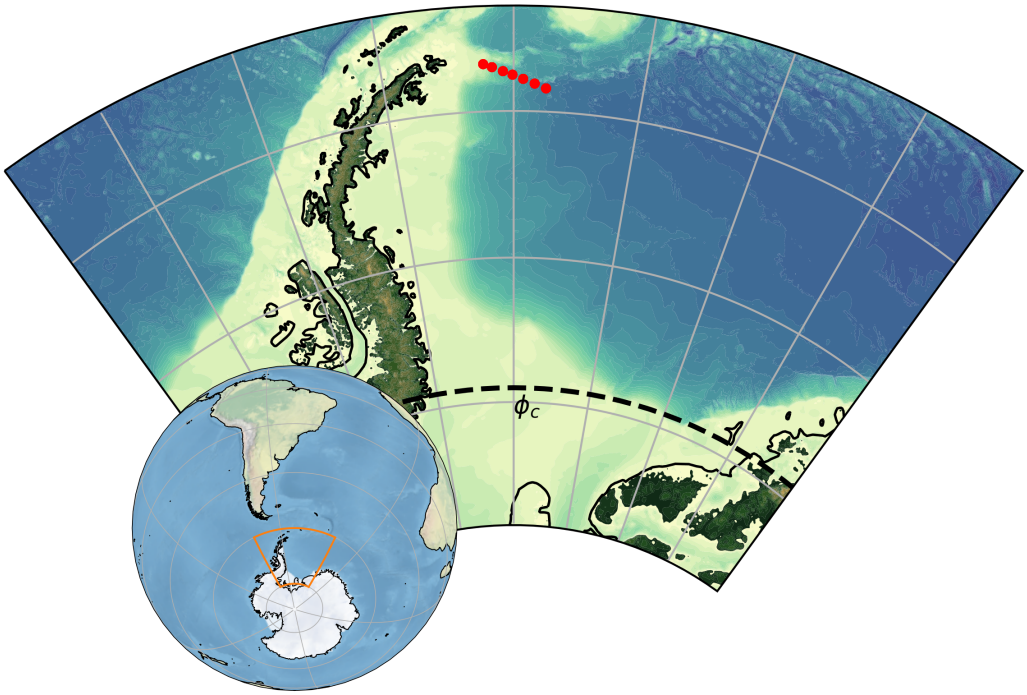

Figure 1: The Weddell Sea. The locations of the moorings are drawn in red. The dashed line denotes the critical latitude of the M2 tide at 74.5 °S, but is not yet of any further importance here.

on the Southern Hemisphere, the Coriolis force always point to the left. Steered like that, the dense water does not flow directly down slope, but follows the topography along the continental shelf break in front of the Antarctic peninsula. The Alfred-Wegener Institute deployed 7 moorings (see map in figure 1) around a latitude of 64 °S in an array across the continental slope to capture the Weddell Sea bottom water gravity current before it leaves to the Scotia Sea. The bottom layer is usually defined to be colder than −0.7 °C in terms of potential and not in-situ temperature, but as we are not using this definition or temperature data set further the difference is neglected here. Using the correct definition would decrease the temperatures in the very deep moorings, leading to wider core of the gravity current.

As shown in figure 2, above the cold, dense bottom water, the considerably warmer *cold deep water* can be found. Describing the mixing of these 2 water masses is the

goal of this article. The seasonal behavior of the Weddell Sea Gravity Current and connections to climate modes is described in recent studies like [Llanillo et al., 2022].

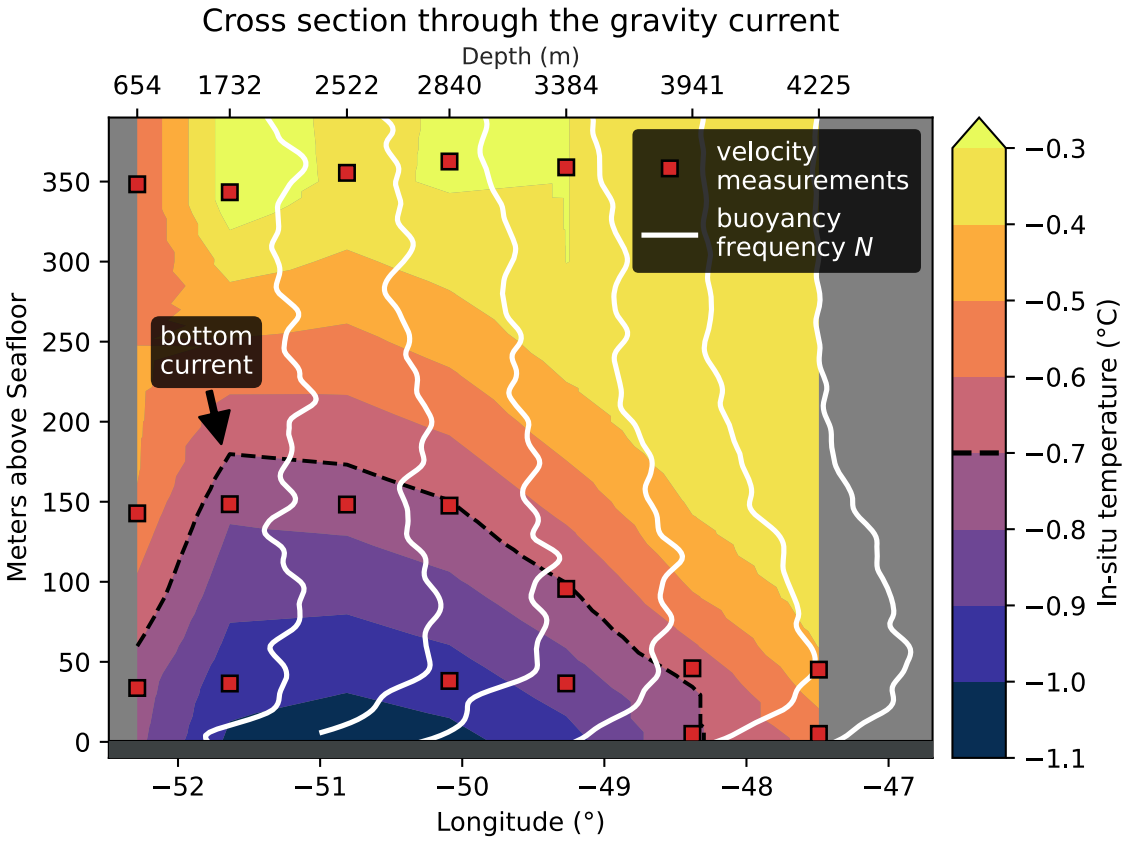

Figure 2: Side view of the gravity current across the continental slope, with the vertical coordinate in *meters above ground*. The numbers above the figure show the depth of the 7 mooring locations. The core of the gravity current can be seen clearly in the in-situ temperature background. The buoyancy frequency N profiles (in white) are calculated in section 5. The red squares denote the average position of the rotor current meters. The mean flow direction is into the page.

3 Mooring and CTD Data set

This work is based on velocity mooring data and CTD profiles in a transect across the continental slope, eastward of the Antarctic peninsula. The 7 moorings are placed in a roughly equidistant pattern on a line from 63.4 °S, 52.3 °W to 64.3 , S47.6 °W. They were all deployed during the Polarstern expedition PS103 during New Year 2016/2017 and recovered during PS117, January 2019. The moorings are equipped with rotor current meters, temperature, and salinity loggers. The mooring temperature data will be here used only for visualizing purposes and to crosscheck the validity of the results from CTD profiles.

The rotor current meters were set to measure the velocity every 2 hours. Except a few shorter records because of battery failure, most here considered velocity data sets are 2 years in total length. Figure 3 shows an example time period of a velocity measurement. The average mean flow points North-west, which is consistent with our expectations for the direction of the gravity current. All except the deepest moorings show aligned mean current directions along the slope, with a slight current speed increase slightly towards the bottom. The strongest mean velocities were measured in the bottom current (at 1700 m and 2800 m water depth), which we interpret as the core of the gravity current, as they also coincide with the lowest temperatures. The variability in current velocity is highest across-slope

The mooring data set is supported by CTD profiles of a vertical resolution of 1 dbar along the same transect which were taken during the mooring deployment on PS103, the mooring recovery PS117 and the PS129 research cruise from 2022.

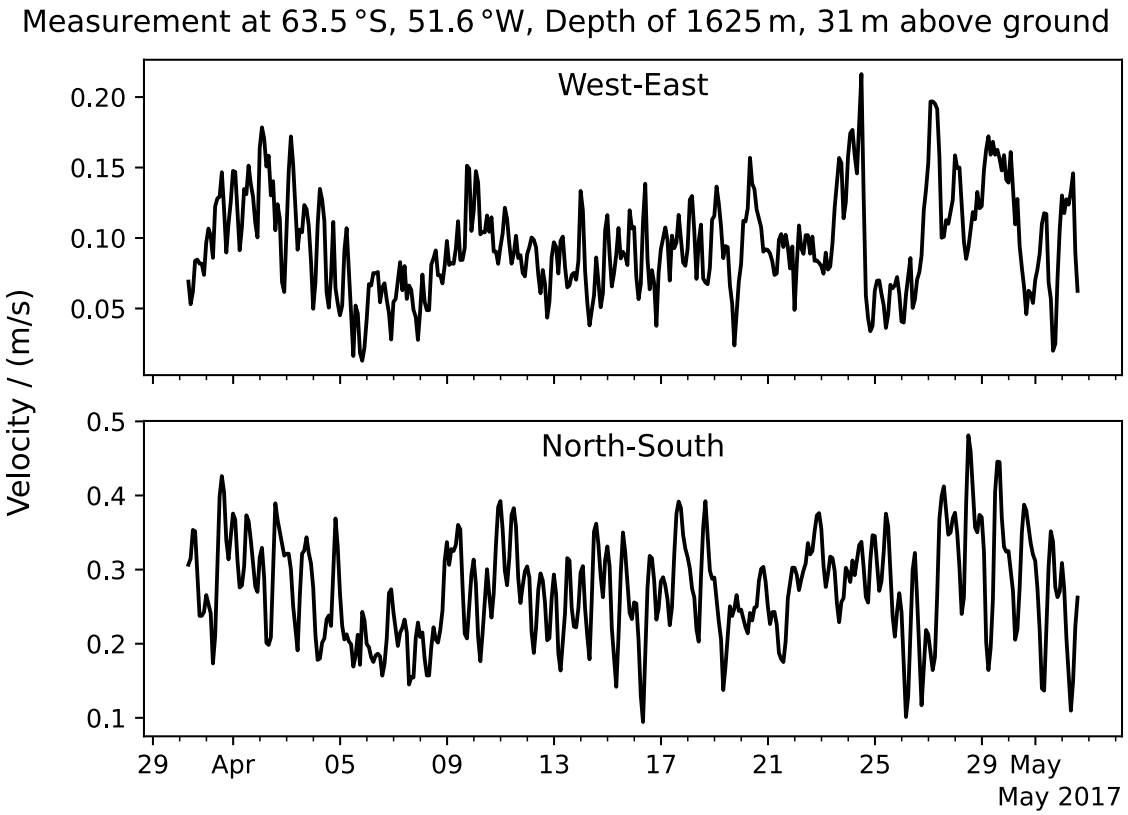

Figure 3: Excerpt of a velocity time series, measured by a rotor current meter. The geographical location and depth position of the instrument is in the figure title. The upper subplot shows the east-west velocity u, the lower subplot the north-east velocity v, both in units of $\mathrm{m\,s^{-1}}$.

4 Energy levels

We calculate the velocity spectra from the measured velocities with a multitaper of product-bandwidth $P = 10$, which controls the internal averaging window. The current velocity measurements, every 2 hours, correspond to a maximum frequency resolution of 6 cpd or 6.9×10^{-5} Hz. The resolution of long-term oscillations depends on the time series length, which differs between the various instruments. But in the following calculations, no data with lower frequencies than 1 cycle per day is used. The accuracy of the multitaper method can be checked by integrating the full spectrum and comparing the result to the kinetic energy from the time series $\mathrm{KE} = {}^1\!/_2\overline{(u^2 + v^2)}$, as the change from the time to the frequency domain should not lose energy.

An example spectrum can be found in figure 4. The general background shape is a plateau at low frequencies and then a decay towards high frequencies. On top of the background are peaks, especially at 1 and 2 cycles per day, which are of tidal origin. Non-tidal waves, slower than f, will transport energy to the internal wave continuum, so just considering the latter here is sufficient for any considerations of mixing.

4.1 Internal Tides vs Internal Wave continuum

For every frequency of the most important tidal frequencies (M2, S2, N2, K2, K1, O1, P1, Q1), chosen to be the same as in [Padman et al., 2002], we define a frequency ν range dependent on the multitaper product bandwidth P

$$[\nu_{i-P}, \nu_{i+P}]$$

as the peak width[2]. Overlapping frequency ranges around close tidal frequencies are combined. A value for the background spectrum is defined as

$$\min\Big(\mathrm{PSD}(\nu_{i-P}), \mathrm{PSD}(\nu_{i+P})\Big) \quad .$$

Subtracting the energy because of the tidal peaks, that fall in the frequency range between the Coriolis frequency f and the buoyancy frequency N, from the energy total energy of the same range, yields the energy level of the internal wave continuum. As seen in the figures 7 and 8, the buoyancy frequency N is here of order of magnitude of 1×10^{-3} Hz or 86 cpd. As we cannot resolve up to N, the integral is just until the maximum resolved frequency. As the power density spectra decay by several orders of magnitude over the range of the internal wave continuum, we neglect the non-resolved energy.

[2]In the python code, this corresponds to $[\nu_{i-P}, \nu_{i+P+1})$.

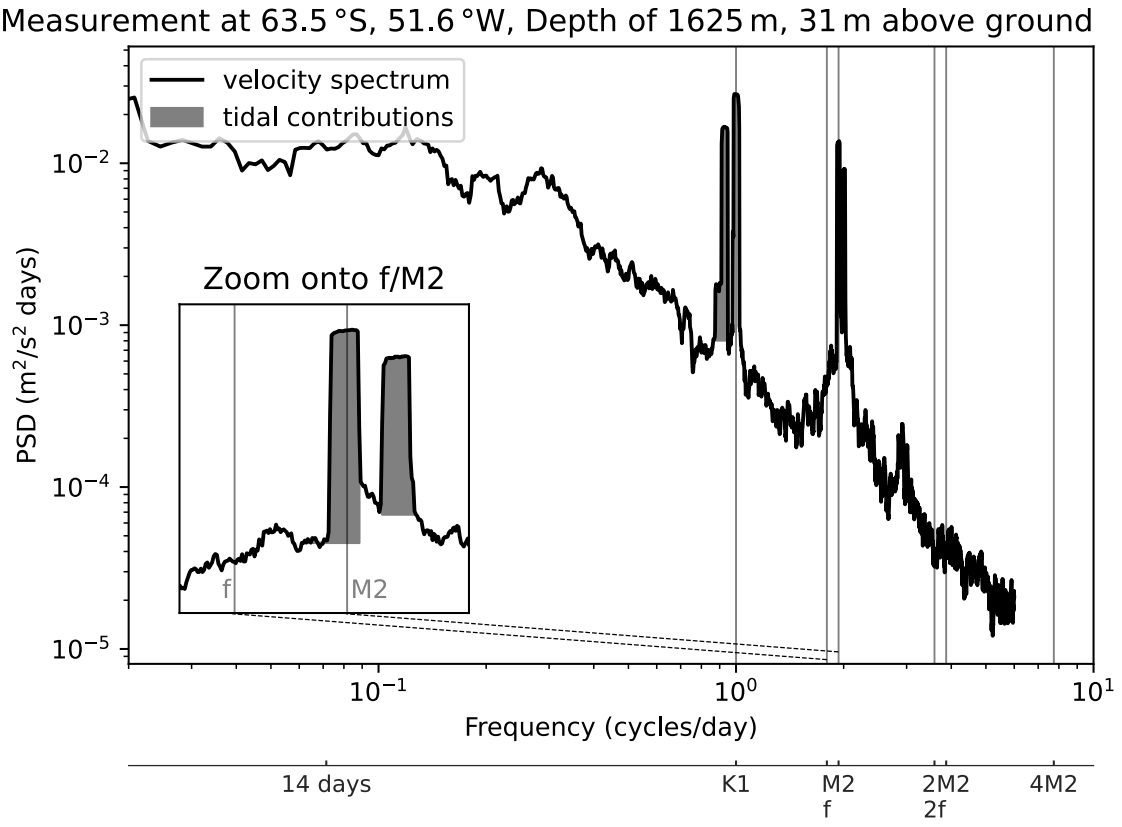

Figure 4: Multitaper spectrum of the velocity measurement, of which an example is displayed in figure 3. The inset plot shows a zoom onto the 2 cycles per day frequency, which f and the M2 tide frequency are very close to. The gray colored areas are what we define as tidal contributions to the total energy on top of a smooth internal wave continuum background.

4.2 Barotropic vs Baroclinic tides

To differentiate the total tidal energy further into barotropic and baroclinic components, we look into the depth dependency of the velocity measurements. To get a benchmark to compare to, we assume the shallowest velocity measurement of each mooring is purely barotropic, and any baroclinic tide increases the total tidal energy towards the bottom. This approach has several problems. First, the shallowest measurement of each mooring is different and ranges from 360 m to 40 m above the sea floor and second, we need at least 2 mooring spectra per water column, which is not given for the mooring at 64.1 °S, 48.4 °W. Any distinction between the nature of tidal oscillations is not possible without any vertical information. And at last,

the assumption of higher energy levels closer to the seafloor doesn't always hold (see figure 6).

Therefore, our result can only be our best guess of the real barotropic tide. Nonetheless, we can check this calculation approach against the barotropic tidal energy from the Circumpolar Antarctic Tidal Simulation (CATS) model from [Padman et al., 2002, Howard et al., 2019] and from a harmonic fit to the measured velocity time series using ttide_py [Pawlowicz et al., 2002].

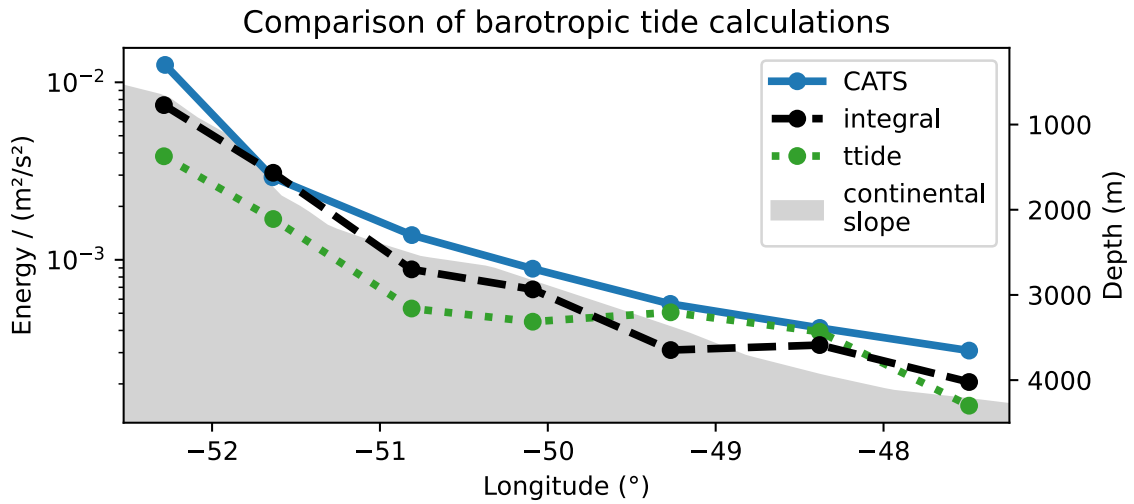

Figure 5: Comparison of the 3 different estimates for the barotropic tide across the continental slope.

All methods agree on the general pattern of decaying tidal strength towards the deep sea. The high values on the shelf for the barotropic tide in the CATS model may stem from incorrect bathymetry data, but across the whole slope the numeric model predicts higher energies than our data can confirm. The ttide method is vulnerable to phase shifts in the data due to drifting internal clocks and low signal-to-noise ratios. Combined, the ttide method probably underestimates the barotropic tide slightly. In conclusion, the approach of integrating the tidal peak in the spectra to get the tidal energy may be the most accurate approach here, although not without its own flaws and problems.

4.3 Distribution of Kinetic Energy

Figure 6 shows the calculated energy levels for the barotropic tide, the baroclinic tide and the internal wave continuum across the continental slope. All shown wave

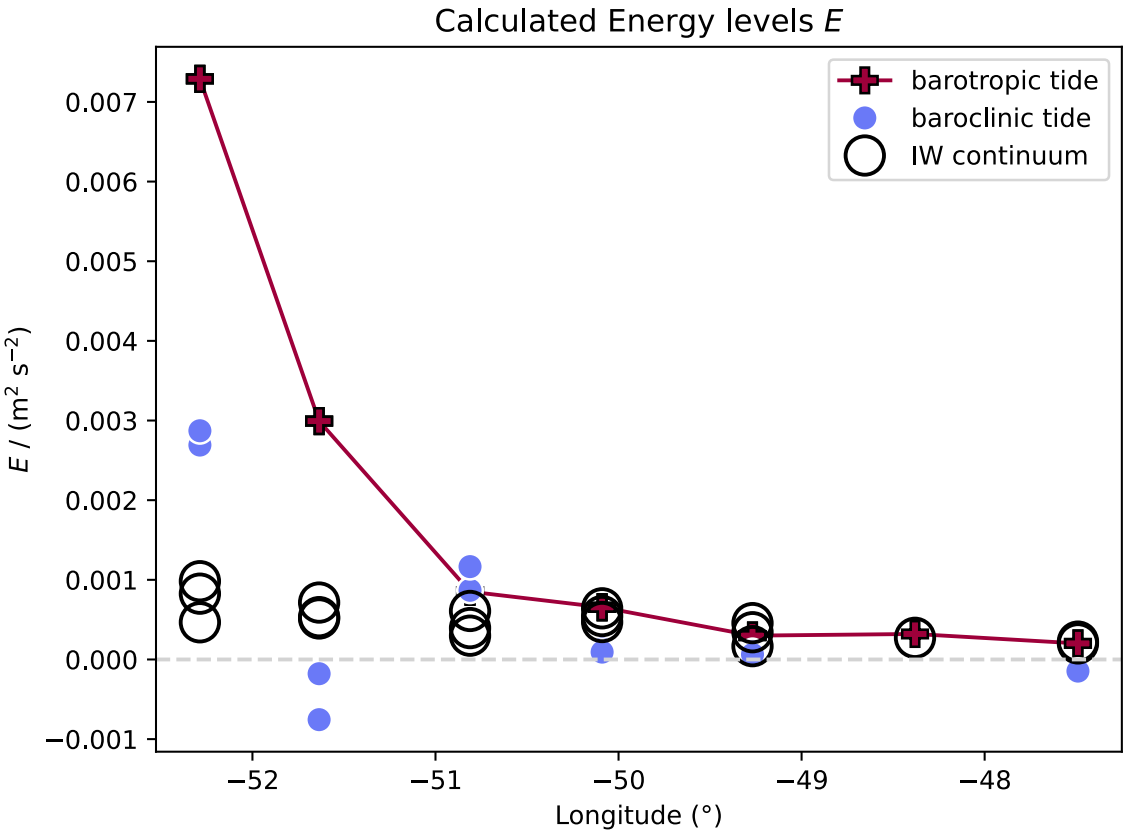

Figure 6: Calculated kinetic energy distribution across the continental slope. For 2 moorings, our approach of assuming of increasing energy towards the sea floor fails, resulting in non-physical baroclinic negative energies.

types are elevated on the shelf, with the barotropic tide showing the highest decrease in strength across the slope. Notably, the energy of low frequency oscillations (not depicted) are stronger towards the deep sea, despite weaker mean currents and lower high frequency wave activity. For the moorings at 63.5 °S, 51.6 °W and 64.2 °S, 47.5 °W, our approach of assuming of increasing energy towards the sea floor fails, resulting in non-physical baroclinic negative energies. These 3 data points are removed in further calculations.

It is not obvious how to determine the error of the kinetic energy, as the biggest error stems probably from invalid assumptions which are difficult to quantify. One possibility could be to consider the spread of barotropic energy estimation for each of the mooring locations as the uncertainty. which propagates to the calculation of the baroclinic energy.

5 Buoyancy frequency N

Just the knowledge of energy levels is not enough for quantifying mixing, as that depends also on the stratification. Although the data from 7 moorings also include long-term temperature time series, they are not applicable here as their vertical resolution is too coarse. CTD profiles are much higher spatially resolved, but lack the temporal coverage. To mitigate this effect, we combine CTD data from the deployment cruise PS103, the recovery cruise PS117 and the more recent PS129 cruise across the same section.

For every mooring location, we select CTD profiles from PS103, PS117 and PS129, which were taken no further than 70 km away. This results in 7 to 9 CTD profiles each, most of which are in close range to the desired mooring locations. To compensate the slightly different water depths at the profile locations, for every mooring location the z-axis of all corresponding profiles are converted to be distance from the sea floor and aligned. Any irregularities closer to the sea surface can be ignored, as we are only interested in the processes and data close to the continental slope.

The squared buoyancy frequency is calculated with the GSW toolbox for python. All N profiles were smoothed by convolution with a 32 points wide Hanning window and averaged to give an estimation for the average stratification.

The stratification at the shallowest mooring shows the highest variability, as surface processes still have an influence. Further down slope, the bottom current increases the stratification above the background value as far as 600 m from the sea floor. Towards the deep sea, the height of the gravity current decreases down to approximately 200 m. Closer than 50 m to the sea floor, N drops almost rapidly, as bottom friction lead to a homogenized bottom boundary layer.

The statistical error in the calculation of the mean profiles is the standard deviation of the averaging, although it rather represents natural variability than any measurement error. Qualitatively, the spread of the data can be seen in the faint gray N profiles in figure 7.

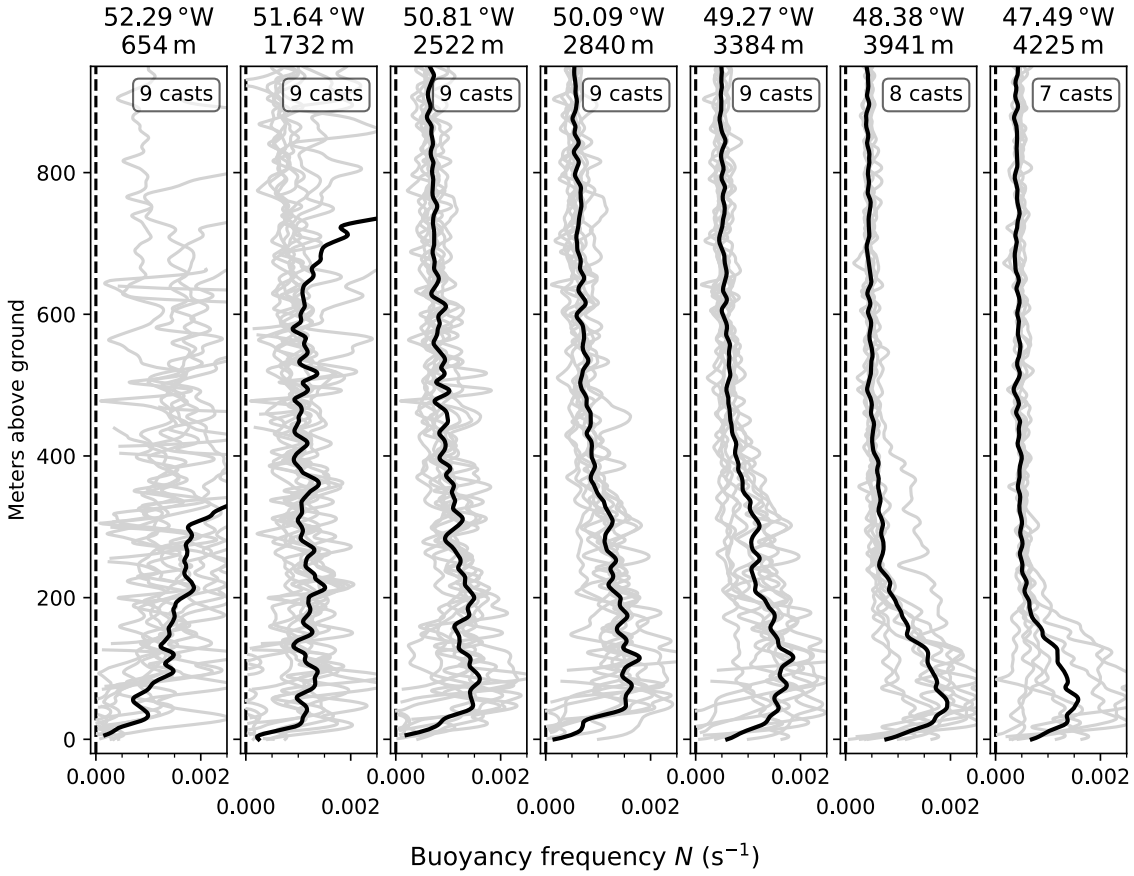

Figure 7: Buoyancy frequency N close to the sea floor across the continental slope. The black lines denote the smoothed average profiles, while the faint gray are the smoothed individual CTD profiles, ranging from 7 to 9 CTD profiles per mooring location.

6 Diapycnal Diffusivity

The next step is to combine the previous results of sections 4 & 5 and calculate the diapycnal diffusivity. For that we follow [Olbers and Eden, 2013, eq. 18].

$$K_\rho \approx \frac{\Gamma}{1+\Gamma}\mu_0 f_e \frac{m_\star^2 E^2}{N^4} \tag{1}$$

Buoyancy frequency	N		from CTD data
Energy level	E		from velocity spectra
Mixing efficiency	Γ	$=$	0.2
Coriolis frequency	f	$\approx$	$-2.08 \times 10^{-5}\,\mathrm{Hz}$
Effective f	f_e	$=$	$\lvert f\rvert \operatorname{arccosh}(N/\lvert f\rvert)$
Spectral bandwidth	$m_\star$	$=$	$0.01\,\mathrm{m}^{-1}$
	μ_0	$=$	$2/3$

This equation assumes that non-linear interactions between waves always transport energy towards smaller wave numbers at a rate independent of the wave number itself. Therefore, to calculate how much energy leave the internal wave background to turbulence, it is possible to also look at higher wave numbers instead. This approach is only valid for the baroclinic tidal energy and the energy of the internal wave continuum and explicitly does not apply to barotropic tides, as they are not internal gravity waves. We can associate every depth of each energy level to a N value. The results for the buoyancy frequency from section 5 are smoothed even further to remove statistical variability along the depth axis completely. The spectral bandwidth $m_\star$ could be dynamically computed by fitting the Garret-Munk model to each spectrum, but it is here only used as a constant.

Because the mooring data has almost no vertical information, we cannot distinguish between high modal baroclinic tides, which break and lose energy and low modal, which energy is not yet available for mixing. Therefore, we consider both cases, including and excluding internal tides, separately. Without the tides, we disregard energy, giving us a conservative estimate of the wave mixing. Including the baroclinic tidal energy overestimates because of the prevalence of low modes. A future step could be to look at lowered ADCP profiles to estimate the energy ratio of low and high tidal modes.

Figure 8 shows the results of the diffusivity calculation. Despite the gaps in the data of the baroclinic tide, we observe stronger tidal mixing in shallow regions. We can also see a smaller increase on the shelf in the mixing due to the internal wave

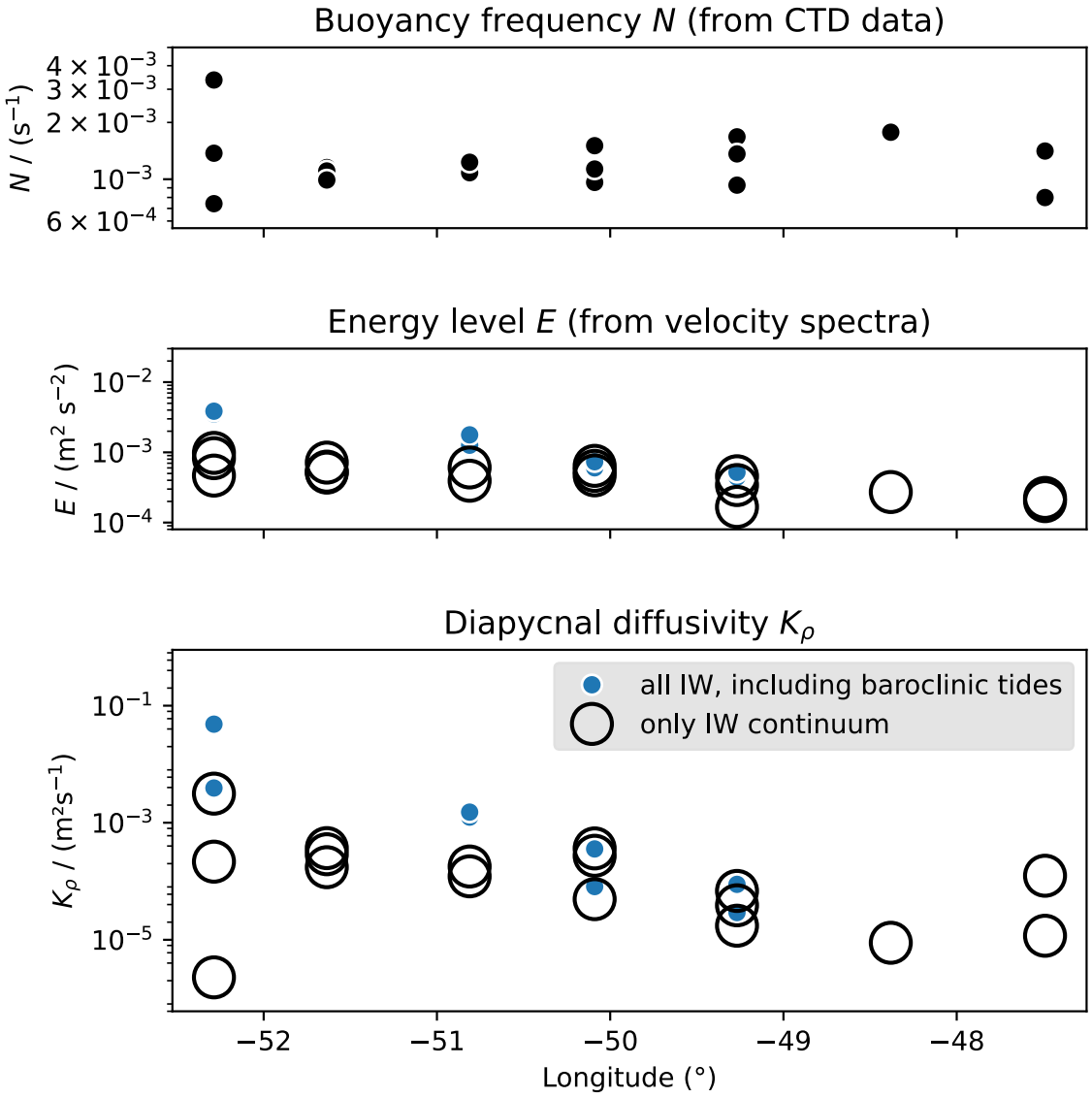

Figure 8: Outcome of the calculation of energy levels and buoyancy frequency described in 4 and 5 and the resulting diffusivity K_ρ from equation 1. The energy levels and diffusivity distinguish between including (in blue) and excluding (in black) the baroclinic tide.

continuum. As both estimates give us a range for the real diffusivities, the areas of the highest mixing coincide with the highest uncertainty. To further quantify the uncertainty of these results, we can propagate the error from the previous sections for E and N, which as of right now is not done yet.

7 Conclusion

Our results reveal the distribution of wave energy levels across the Weddell Sea bottom water gravity current. The internal wave mixing between the Weddell Sea Bottom Water and Warm Deep Water is around 2 orders of magnitude stronger in the shallower regions towards the Antarctic continent. The largest relative and absolute tidal contribution to the wave mixing is on the shelf. There, the possibility of underestimating the internal mixing by disregarding internal tides is especially prevalent. Numerical models cannot relay on a background diffusivity here if they are not eddy allowing enough, which global or even most regionals models certainly are not.

If we compare our results to literature values for measured diffusivities, we find that close to the Filchner-Ronne ice shelf, southwards of the critical latitude ϕ_C, [Fer et al., 2016] observed a bottom layer of 100 m thickness, in which dissipation rates up to $1 \times 10^{-7}\,\mathrm{Wkg}^{-1}$ or $K_\rho = 1 \times 10^{-2}\,\mathrm{m^2s^{-1}}$ were measured with a microstructure profiler. [Fer et al., 2016] gives the explanation that a semidiurnal internal tide generated on the upper continental slope is the reason for these high diffusivities. Due to the vicinity to the critical latitude, it cannot propagate and dissipates its energy in the bottom boundary layer. They suggest a spatial scale of this mechanism in the order of 10 km. In front of Cape Darnley, another formation site of Antarctic Bottom water, eastward of the Weddell Sea, [Hirano et al., 2015] used microstructure profilers in a gravity current to get diffusivity values of $K_\rho > 1 \times 10^{-3}\,\mathrm{m^2s^{-1}}$ in a bottom boundary layer with a vertical scale of 10 m. They state that turbulent activity starts to strongly increase closer than 30 m towards the bottom. Although they measured higher mixing, their vertical layer scales are an order of magnitude smaller than what the range in that we observe increased turbulence. Further down slope the Weddell Sea gravity current, towards the Scotia Sea, mixing will probably predominantly be due to other processes. [Naveira Garabato et al., 2019, Spingys et al., 2021] state diffusivity values of $K_\rho > 1 \times 10^{-2}\,\mathrm{m^2/s}$ in the bottom 1000 m, created by symmetric instabilities.

Finally, the next step for our work is to place these results in context with estimates for the total mixing from CTD profiles using the Thorpescale and finestructure method.

8 References

[de Lavergne et al., 2019] de Lavergne, C., Falahat, S., Madec, G., Roquet, F., Nycander, J., and Vic, C. (2019). Toward global maps of internal tide energy sinks. *Ocean Modelling*, 137:52–75.

[Fer et al., 2016] Fer, I., Darelius, E., and Daae, K. B. (2016). Observations of energetic turbulence on the Weddell Sea continental slope. *Geophysical Research Letters*, 43(2):760–766. Publisher: Blackwell Publishing Ltd.

[Hirano et al., 2015] Hirano, D., Kitade, Y., Ohshima, K. I., and Fukamachi, Y. (2015). The role of turbulent mixing in the modified Shelf Water overflows that produce Cape Darnley Bottom Water. *Journal of Geophysical Research: Oceans*, 120(2):910–922.

[Howard et al., 2019] Howard, S. L., Erofeeva, S., and Padman, L. (2019). CATS2008: Circum-Antarctic Tidal Simulation version 2008.

[Lenton et al., 2008] Lenton, T. M., Held, H., Kriegler, E., Hall, J. W., Lucht, W., Rahmstorf, S., and Schellnhuber, H. J. (2008). Tipping elements in the Earth's climate system. *Proceedings of the National Academy of Sciences*, 105(6):1786–1793.

[Llanillo et al., 2022] Llanillo, P. J., Kanzow, T., Janout, M. A., and Rohardt, G. (2022). The Deep-Water Plume in the northwestern Weddell Sea, Antarctica Mean state, seasonal cycle and interannual variabilty influenced by climate modes.

[Menezes et al., 2017] Menezes, V. V., Macdonald, A. M., and Schatzman, C. (2017). Accelerated freshening of Antarctic Bottom Water over the last decade in the Southern Indian Ocean. *Science Advances*, 3(1). Publisher: American Association for the Advancement of Science.

[Naveira Garabato et al., 2019] Naveira Garabato, A. C., Frajka-Williams, E. E., Spingys, C. P., Legg, S., Polzin, K. L., Forryan, A., Abrahamsen, E. P., Buckingham, C. E., Griffies, S. M., McPhail, S. D., Nicholls, K. W., Thomas, L. N., and Meredith, M. P. (2019). Rapid mixing and exchange of deep-ocean waters in an abyssal boundary current. *Proceedings of the National Academy of Sciences*, 116(27):13233–13238.

[Olbers and Eden, 2013] Olbers, D. and Eden, C. (2013). A Global Model for the Diapycnal Diffusivity Induced by Internal Gravity Waves. *Journal of Physical Oceanography*, 43(8):1759–1779.

[Padman et al., 2002] Padman, L., Fricker, H. A., Coleman, R., Howard, S., and Erofeeva, L. (2002). A new tide model for the Antarctic ice shelves and seas. *Annals of Glaciology*, 34:247–254.

[Pawlowicz et al., 2002] Pawlowicz, R., Beardsley, B., and Lentz, S. (2002). Classical tidal harmonic analysis including error estimates in MATLAB using T_tide. *Computers & Geosciences*, 28(8):929–937. Publisher: Pergamon.

[Pollmann, 2020] Pollmann, F. (2020). Global characterization of the ocean's internal wave spectrum. *Journal of Physical Oceanography*, 50(7):1871–1891. Publisher: American Meteorological Society.

[Spingys et al., 2021] Spingys, C. P., Naveira Garabato, A. C., Legg, S., Polzin, K. L., Abrahamsen, E. P., Buckingham, C. E., Forryan, A., and Frajka-Williams, E. E. (2021). Mixing and Transformation in a Deep Western Boundary Current: A Case Study. *Journal of Physical Oceanography*, 51(4):1205–1222.